remote sensing

MDPI

Article

Integrating Gross Error Identification with Deep Learning for InSAR Topography-Dependent Delay Correction: A Case Study of the Baihetan Hydropower Station Area

Yuanyuan Liu [1,2], Hongli Chen [1,*], Dan Liu [1,2] and Bo Liu [1,2]

[1] School of Surveying and Geoinformation Engineering, East China University of Technology, Nanchang 330013, China; yuanyuan_0106@ecut.edu.cn (Y.L.); 201660018@ecut.edu.cn (D.L.); liubo@ecut.edu.cn (B.L.)
[2] Key Laboratory of Mine Environmental Monitoring and Improving Around Poyang Lake of Ministry of Natural Resources, East China University of Technology, Nanchang 330013, China
* Correspondence: 2024120596@ecut.edu.cn

Highlights

What are the main findings?

- Deep learning architectures, such as the MLP model, significantly outperform conventional phase-based or meteorological model-based methods in the modeling and correction of tropospheric delay.
- Phase unwrapping gross errors existing in the interferograms adopted for deep learning model training will inevitably degrade the modeling accuracy, which cannot be neglected in practical applications over complex mountainous regions.

What are the implications of the main findings?

- The integration of the gross error identification module into the MLP model establishes a generic framework, which effectively mitigates the dependence of deep learning models on high-quality phase unwrapping results.
- The EiMLP method combines phase information with deep learning methods, which provides a novel solution for tropospheric delay correction in complex mountainous regions.

Abstract

Tropospheric delay poses a major limitation to high-precision InSAR observations, particularly in high mountain and canyon regions. To address this issue, this study proposes a combined model (EiMLP) that integrates gross error identification with a multilayer perceptron (MLP) for topography-dependent tropospheric delay correction. The gross error identification module detects unwrapped phase jumps based on phase gradients, followed by an MLP model that reconstructs the atmospheric phase using unwrapped phase and elevation information from a single interferogram. The proposed method is validated in the Baihetan Hydropower Station area and compared with traditional correction methods. Experimental results demonstrate that the proposed method achieves a Structural Similarity Index Measure (SSIM) of 0.970 and a Root Mean Square Error (RMSE) of 0.673 rad for the simulated atmospheric phase. After atmospheric correction, the average phase standard deviation of the interferograms is reduced by 83%, and the topography-related correlation is significantly suppressed. Furthermore, after correction by the proposed method, the signals that are masked by atmospheric errors in the original interferograms can be clearly revealed, indicating the potential for slope instability. These findings indicate

Check for updates

Academic Editor: Antonio Miguel Ruiz Armenteros

Received: 7 May 2026
Revised: 18 June 2026
Accepted: 1 July 2026
Published: 3 July 2026

Copyright: © 2026 by the authors. Licensee MDPI, Basel, Switzerland. This article is an open access article distributed under the terms and conditions of the Creative Commons Attribution (CC BY) license.

that the EiMLP model, operating on a single interferogram, exhibits robust applicability and provides a reliable reference for future InSAR tropospheric delay correction.

Keywords: InSAR; topography-dependent atmospheric correction; deep learning; gross error identification; GACOS

1. Introduction

Interferometric Synthetic Aperture Radar (InSAR) has been widely applied in landslide monitoring due to its all-day, all-weather, high-precision characteristics [1–3]. However, monitoring accuracy is inevitably affected by various errors, among which atmospheric errors are one of the main error sources.

According to atmospheric stratification theory, atmospheric artifacts can be divided into ionospheric and tropospheric delays. Among them, tropospheric delay serves as the dominant influencing factor for C-band (i.e., Sentinel-1A) signals in mid- to low-latitude regions, while ionospheric delay remains relatively small and can be neglected. Therefore, the primary objective of this paper is to mitigate the tropospheric delay errors. Based on physical characteristics, tropospheric delay errors can be further classified into vertically stratified delay and turbulent delay. Vertically stratified delay is mainly induced by vertical variations in the atmospheric refractive index, showing a strong correlation with topographic conditions. In contrast, turbulent delay driven by the complex interactions of diverse turbulent mixing processes, exhibits highly irregular spatiotemporal variations [4,5].

Currently, numerous methods for correcting tropospheric delay errors have been proposed. The first category is the correction methods based on external auxiliary data, such as numerical weather models [6], the Generic Atmospheric Correction Online Service for InSAR (GACOS) [7–9], the Global Navigation Satellite System (GNSS) [10–13], and combinations thereof [14]. The second category focuses on the phase-based correction methods, including spatiotemporal filtering [15,16], interferogram stacking [17,18], hybrid models [19–22], and heterogeneity models constructed considering atmospheric physical properties [23–26].

When the atmospheric errors over the study area are topography-dependent and dominated in the vertical direction, the atmospheric refractive index decreases with increasing altitude, thereby generating additional delay phases. This delay propagates along the line of sight and is superimposed on the real signal, resulting in deviations in the measurements. Such errors are highly correlated with terrain and vary dramatically with terrain undulations; the aforementioned methods fail to meet practical requirements. Specifically, GACOS generally performs poorly in complex mountainous areas and is susceptible to inconsistencies in spatial resolution, whereas the correction accuracy of GNSS-based methods is constrained by the spatial density of monitoring stations. In recent years, deep learning methods have been employed for tropospheric error correction due to their outstanding feature learning ability. However, each algorithm has inherent limitations, rendering some models inapplicable to the correction of vertically stratified tropospheric delays. For example, the GRU network has a model structure suitable for capturing temporal relationships in time series, but it cannot truly isolate tropospheric delay; the ARU-NET model, combined with an attention mechanism, can capture turbulent delay, but it still cannot reliably distinguish between deformation and vertical stratification delay [27–29]. Moreover, the correction method based on the MLP model is highly sensitive to phase unwrapping errors in terms of accuracy. In practice, these factors need to be manually investigated [30–32].

This paper proposed a topography-dependent atmospheric correction method based on EiMLP neural network, by integrating gross error identification and the multilayer perceptron (MLP) algorithm. The proposed method was applied to the Baihetan Hydropower Station area, which suffered from severe topography-dependent atmospheric artifacts. The correction performance was quantitatively compared with that of the global linear model, GACOS product and standard MLP model. The results verified its promising practical value for improving InSAR monitoring accuracy and facilitating effective geological disaster detection.

2. Materials and Methods

2.1. Study Area and Data

2.1.1. Overview of the Study Area

To evaluate the performance of the proposed method, the Baihetan Hydropower Station was chosen as the study area (Figure 1), which spans Ningnan County, Sichuan Province (27.04°N, 102.9°E), and Qiaojia County, Yunnan Province (26.78°N, 103.12°E). Situated on the southeastern margin of the Qinghai–Tibet Plateau, the region has an elevation ranging from 1000 m to 3000 m. Geomorphologically, it pertains to the alpine-plateau landform unit and the Hengduan Mountain system across southwestern Sichuan and northeastern Yunnan. Dramatic topographic relief creates obvious vertical climatic zonation, covering climate zones from southern subtropical to cold temperate. Local landforms are primarily shaped by fluvial erosion, tectonic movement and glacial erosion, characterized by deeply incised valleys and intense weathering and denudation [33,34]. As illustrated in Figure 1, the reservoir is located in the lower Jinsha River basin, and the overall terrain is high in the east and low in the west. Steep bank slopes, lofty mountains and deep gorges are widely distributed, and the river valley is dominated by typical V-shaped landforms, forming a representative alpine and deep-canyon landscape. The impoundment of the reservoir induces a sharp rise in water level, which further triggers frequent geological disasters such as landslides, debris flows and rock collapses. In the study area, landslides occur frequently, with hundreds of unstable slopes. Due to periodic fluctuations in reservoir water levels, rainfall, and human activities, typical examples include the Xiaomidi, Gantianba, and Wulipo landslides, which seriously affect human activities and life safety. In this context, high-precision displacement monitoring is particularly essential for regional hazard prevention [34–36].

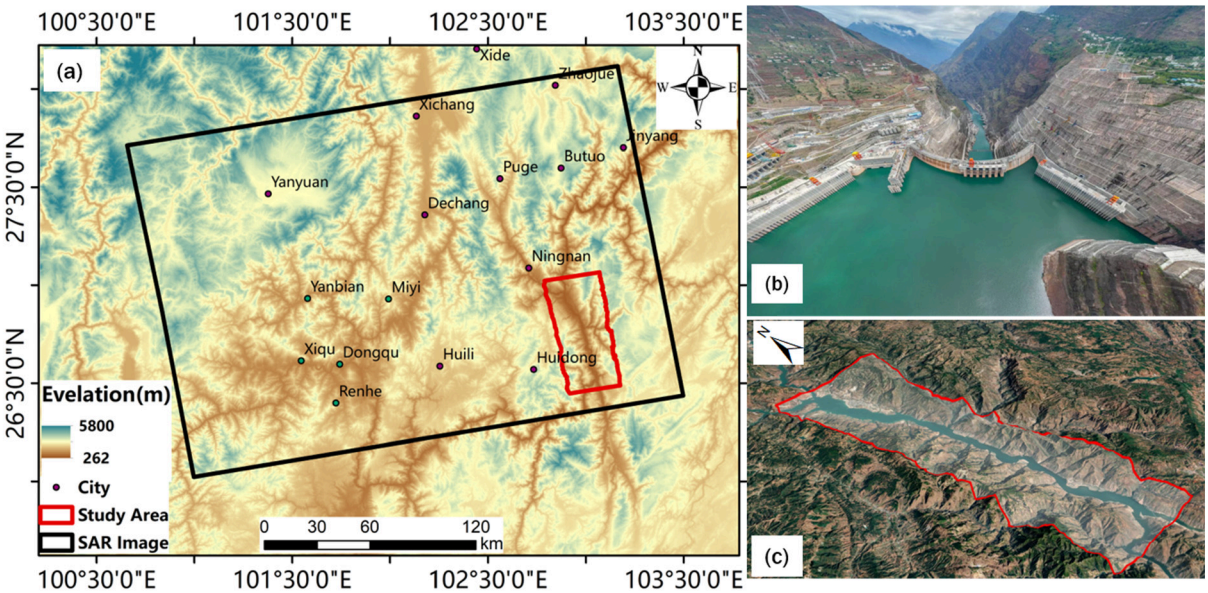


Figure 1. (**a**) Geographical location map of the study area, (**b**) photo of the Baihetan Hydropower Station, (**c**) remote image of the study area from Google Earth.

2.1.2. Dataset

This study utilized 30 C-band ascending Sentinel-1A SAR images covering the Baihetan Hydropower Station area, provided by the European Space Agency (ESA). The datasets were collected from May to November in 2019 and 2021. These images were captured in Path 26 with a 12-day revisit time under the Interferometric Wide (IW) swath mode, featuring VV polarization and a satellite azimuth angle of 347.5°.

To suppress spatiotemporal decorrelation and minimize interference of surface deformation, the temporal baseline of interferometric pairs was restricted within 24 days. After removing the low-quality pairs, 28 qualified interferograms were used for subsequent analysis. The detailed information of these interferogram pairs is listed in Table 1.

Table 1. Interferogram pairs used for experiment.

Interferogram Pairs	Interferogram Pairs
20190502–20190514	20191029–20191122
20190502–20190526	20210421–20210503
20190526–20190607	20210503–20210515
20190526–20190619	20210503–20210527
20190619–20190701	20210527–20210608
20190806–20190818	20210608–20210620
20190806–20190830	20210608–20210702
20190911–20190923	20210620–20210702
20190911–20191005	20210807–20210819
20190923–20191005	20210807–20210831
20191005–20191017	20210819–20210831
20191017–20191029	20210912–20210924
20191017–20191110	20210912–20211006
20191029–20191110	20211018–20211030

Moreover, the Copernicus Digital Elevation Model with a resolution of 30 m was applied to remove the topographic and flat phase from the interferogram, which is a global DEM dataset released by the ESA and is widely recognized as one of the highest-quality open-source elevation products to date. It is generated from radar observations acquired by the German Aerospace Center (DLR) through the TanDEM-X mission with data acquisition conducted between 2010 and 2015. Its performance in complex terrain areas significantly outperforms traditional DEM products such as the NASA DEM [37].

2.2. Methods

2.2.1. Tropospheric Delay Mitigation by EiMLP

(1) Gross error identification

Gross error identification was implemented by calculating the pixel-wise phase gradient. Empirical results have demonstrated that obvious boundaries of phase unwrapping errors can be clearly distinguished when the gradient between adjacent pixels exceeds 1 rad. Accordingly, the detection threshold was set to 1 rad, and a sliding window strategy was utilized for gross error identification. In the identification process, the phase differences between a given pixel and its right and lower neighboring pixels were calculated for each input individual interferogram. A gross error was flagged once either of the following conditions was satisfied:

$$\Delta\phi(i,j) = |\phi(i,j+1) - \phi(i,j)| > 1 \quad (1)$$

$$\Delta\phi(i,j) = |\phi(i+1,j) - \phi(i,j)| > 1 \quad (2)$$

In this paper, the window moved pixel by pixel with a step size of 1. Whenever the sliding window encountered a pixel with a gross error flag, all valid pixels within the current window were masked and excluded from subsequent model training. Subsequently, the window moved to the next valid pixel, and the above operation was repeated until the entire interferogram had been fully traversed and the termination condition was met.

(2) Tropospheric delay mitigation by MLP model

In the field of deep learning, there is a category of novel architectures that completely abandons convolution and the self-attention mechanism, and only performs feature extraction and mapping based on the MLP layers [38]. The MLP model adopted in this study comprised ten fully connected layers with an input dimension of 3, corresponding to three key geographic variables: elevation, longitude, and latitude. The output was a single channel that characterized the predicted atmospheric phase. From the input interferogram, the model extracted multi-dimensional information including longitude, latitude, elevation and phase values. It further captured the inherent correlation between topographic elevation and atmospheric phase through the fully connected layers, and finally generated the estimated tropospheric delay phase.

The core of the proposed model lay in its forward propagation procedure. Through multi-scale nonlinear transformations, it realized high-precision mapping from low-dimensional geographic features to complex atmospheric phase patterns, which provided an effective numerical modeling tool for tropospheric delay correction. This detailed implementation process can be described as follows:

$$h_1 = Dropout(RELU(W_1 x + b_1)) \tag{3}$$

$$h_i = Dropout(RELU(W_i h_{i-1} + b_i)) \tag{4}$$

$$\hat{y} = w_{10} h_9 + b_{10} \tag{5}$$

where W_i and b_i represent the weight matrix and bias vector of the i layer ($i \in [2, 9]$), and $\hat{y}$ represents the predicted value of the final atmospheric phase.

During the model training process, each pixel from both the interferogram and the corresponding DEM was regarded as an independent training sample. For each sample, the network performed progressive feature compression and information extraction by mapping high-dimensional inputs into lower-dimensional feature representations. Considering that tropospheric delay imposed distinct interference on different interferograms, an independent model was trained separately for each interferogram. The details of the activation function and loss function were presented in Equations (6) and (7), respectively:

$$RELU(x) = \max(0, x) \tag{6}$$

$$WMSE = \frac{1}{n} \sum_{i=1}^{n} w_i \cdot (y_i - \hat{y}_i)^2 \tag{7}$$

where w_i denotes the weight parameter. The weight of each feature can be adaptively adjusted according to its salience, enabling the model to become more sensitive to prominent features during training. n represents the number of samples obtained for the batch size, y_i is the true phase value, and $\hat{y}_i$ is the predicted phase value.

The schematic diagram of the proposed EiMLP method is shown in Figure 2.

2.2.2. Global Linear Model Correction Method

Vertical stratification effects are regarded as quasi-static states over a given region and time period. As the surface elevation increases, vertically stratified tropospheric delays grow alongside rising water vapor content and pressure–temperature ratios [39]. The

concentration of water vapor decreases exponentially with the growing altitude, and the theoretical tropospheric delay follows a similar exponential variation with elevation [40]. When static stratification dominates atmospheric artifacts within an interferogram, the integrated delay component equals the differential delay between the master and slave SAR acquisitions. The exponential elevation-delay function can be simplified via second-order Taylor expansion. By eliminating higher-order terms during simplification, an approximation linear correlation is finally derived, which is presented in Equation (8):

$$\phi = b + kh \tag{8}$$

where b is the bias factor, h is the topography elevation, ϕ is the phase, and k is the transfer function between the topography elevation and phase.

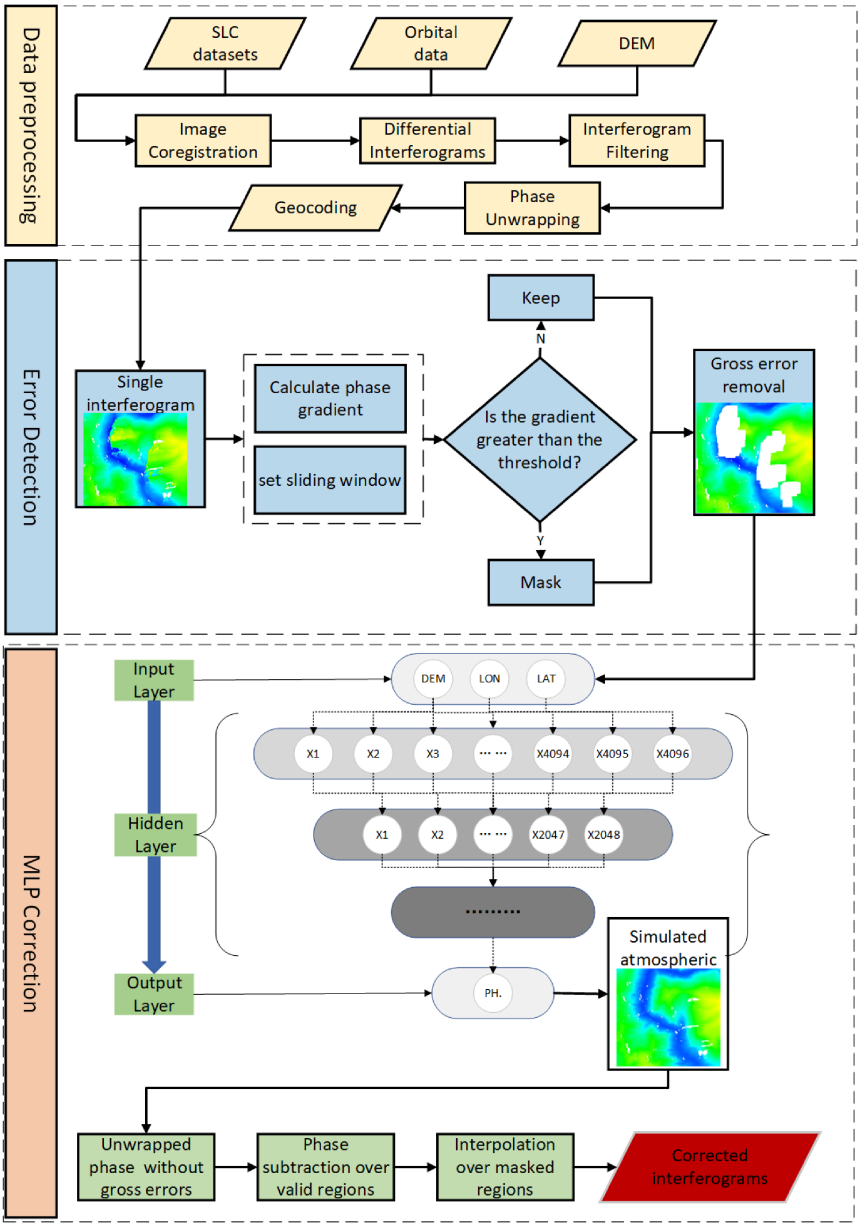


Figure 2. Overview of the proposed EiMLP method.

2.2.3. GACOS Correction Method

GACOS is a globally applicable tropospheric delay correction model with all-weather and year-round capability, and has been extensively validated using interferograms from diverse terrains and climatic zones worldwide [41,42]. After the correction, it can improve

the deformation accuracy to 1 cm [43]. The principle of atmospheric error correction in the GACOS model relies on the Iterative Tropospheric Decomposition (ITD) interpolation algorithm, which decomposes the Zenith Total Delay (ZTD) into elevation-dependent and turbulent components, and further generates high-resolution tropospheric delay maps through spatial interpolation. The process can be described as follows:

$$ZTD_K = S(h_K) + T(x_K) + \varepsilon_K \tag{9}$$

where ZTD_K denotes the integrated ZTD at location K from GNSS stations and ECMWF; S and T represent the vertically stratified component and turbulent component, respectively; and ε denotes the unmodeled residual component. InSAR users can obtain ZTD products for the corresponding periods by submitting the coordinates and SAR image acquisitions of the study area through the official website (https://www.gacos.net/, accessed on 7 March 2026).

2.2.4. Evaluation Metrics

The Pearson correlation coefficient can quantify the linear correlation between two variables, with the value ranging from -1 to 1. In this study, the Pearson correlation coefficient was adopted to analyze the correlation between the interferometric phase and terrain elevation before and after tropospheric correction, thereby quantitatively evaluating the correction performance of the model. The calculation formula for the Pearson correlation coefficient is presented in Equation (10).

$$r = \frac{\sum_{i=1}^{n} (\phi_i - \overline{\phi})\left(h_i - \overline{h}\right)}{\sqrt{\sum_{i=1}^{n} (\phi_i - \overline{\phi})^2} \sqrt{\sum_{i=1}^{n} (h_i - \overline{h})^2}} \tag{10}$$

where n is the total number of pixels, and $\overline{\phi}$ and $\overline{h}$ denote the means of phase and elevation, respectively.

The phase mean and standard deviation can effectively evaluate the phase dispersion of interferograms. In this study, both metrics were adopted to quantitatively evaluate the overall quality of corrected interferograms. The phase standard deviation was calculated as in Equation (11).

$$\sigma = \sqrt{\frac{\sum_{i=1}^{n} (x_i - \overline{x})^2}{n}} \tag{11}$$

where x_i represents the phase value of the i pixel, $\overline{x}$ denotes the mean phase value over the interferogram, and n represents the total number of pixel (i.e., the sample size). In this study, a smaller σ indicates a more stable corrected phase and demonstrates better performance of the correction method in suppressing topography-dependent atmospheric artifacts and noise.

The Structural Similarity Index Measure (SSIM) is a widely adopted measure for quantifying image similarity, as defined in Equation (12). It establishes a mathematical model by comparing the luminance, contrast, and structure features between reference distortion-free images and distorted counterparts. Relying on three core parameters, the image mean (μ), standard deviation (σ), and covariance (σ_{xy}), SSIM decomposes all image distortion into three independent components: luminance variation, contrast difference and structural degradation [44].

$$SSIM(x, y) = \frac{(2\mu_x\mu_y + c_1)(2\sigma_{xy} + c_2)}{(\mu_x^2 + \mu_y^2 + c_1)(\sigma_x^2 + \sigma_y^2 + c_2)} \tag{12}$$

The SSIM index ranges from −1 to 1, where a higher value denotes greater image similarity. In this study, the SSIM index was adopted to quantitatively evaluate the similarity of reconstructed atmospheric phase derived from the correction model.

3. Results

3.1. Data Preprocessing

3.1.1. DInSAR Processing

All Sentinel-1A images were processed via DInSAR technique within a maximum temporal baseline of 24 days, yielding 28 interferograms for the VV polarization, with approximately 30 m after a multi-look operation. The Copernicus Digital Elevation Model was employed to compensate for the topographic phase in the VV-polarized interferograms. Next, phase unwrapping for all interferograms were implemented using the Delaunay Minimum Cost Flow (MCF) method. Following phase unwrapping, orbital refinement and re-flattening operations were conducted to remove residual orbital phases. Ultimately, geocoding was applied to project the unwrapped interferograms into the geographic coordinate system.

3.1.2. EiMLP Processing

As described in Section 2.1, after obtaining the unwrapped interferograms in the geographic coordinate system, gross error identification was performed. In this study, the sliding window size was set to 10 and the interferograms after gross error removal were subsequently input into the MLP model for training. To improve training efficiency, the batch size was set to 512 and the total training epoch was limited to 100, since additional epochs brought no obvious decline in training loss. For rapid and stable optimal convergence, the initial learning rate was set to 0.001. In particular, the learning rate was halved whenever the loss function exhibited no evident improvement within 10 consecutive epochs. During the training, the Adam algorithm was adopted for parameter optimization during training, and the Rectified Linear Unit (ReLU) was deployed as the activation function for all hidden layers. To prevent overfitting, a dropout strategy was employed to randomly deactivate partial neurons during training, which compelled the network to capture robust features and further strengthened the model's generalization performance across the entire study area. Through comparative tests, a dropout rate of 0.1 was determined as the optimal configuration.

3.2. Comparison of the Simulated Phase

The performance of the proposed EiMLP method was compared with that of three conventional methods, namely the global linear model, GACOS and standard MLP. Figure 3 illustrates the comparison of the interferometric phases simulated by these four methods. Considering the typical atmospheric characteristics and the impoundment status of the Baihetan Hydropower Station, six interferogram pairs (20190502–20190514, 20190911–20191005, 20191029–20191110, 20210421–20210503, 20210620–20210702, and 20211018–20211030) were selected for visual comparison, as shown in the first row of Figure 3. A comparison of the interferogram pairs in 2019 and 2021 revealed that the coherence in riverine areas decreased significantly as the impoundment level of the hydropower station rose. During the rainy summer months (e.g., interferogram pairs 20190911–20191005 and 20210620–20210702), the interferograms were substantially more affected by atmospheric errors than those acquired in other periods. The simulated phases obtained from the global linear model, GACOS, standard MLP, and EiMLP were presented in rows 2 to 5 of Figure 3, respectively. The global linear model was unable to construct complete vertically stratified tropospheric delay phases, especially for some components that were opposite to

the main delay trend. Moreover, GACOS lacked sufficiently detailed results. Although it had higher completeness compared to the global linear model, its simulated delay phase in the mountainous area was still too smooth. The phase patterns simulated by the standard MLP showed a high degree of similarity to the original interferometric phase. Compared with the global linear model and GACOS, the proposed EiMLP model achieved more complete reconstruction of vertically stratified tropospheric delay phases. Nevertheless, the difference between the results of EiMLP and standard MLP was negligible from the graphical comparison, thus requiring further quantitative evaluation for detailed analysis.

Table 2 summarizes the quantitative evaluation results of all models on the 28 interferogram pairs in terms of Root Mean Square Error (RMSE) and the Structural Similarity Index Measure (SSIM). The RMSE was adopted to quantify the deviation between the simulated atmospheric phase and the original atmospheric delay, while SSIM was used to evaluate the structural similarity of the simulated phase, where a value closer to 1 indicated higher structural similarity. The results demonstrated that the proposed EiMLP method achieved optimal performance in both RMSE and SSIM, and outperformed all comparison methods.

Table 2. Comparison of statistical metrics for simulated atmospheric phases.

Metrics	RMSE (rad)	SSIM
Global Linear	2.471	0.902
GACOS	1.135	0.938
Standard MLP	0.744	0.963
EiMLP	0.673	0.970

Figure 4 presents a comparison of the simulation results obtained by standard MLP and EiMLP for interferogram pair 20210620–20210702. The area enclosed by the black dashed box indicates the main location of the differences. Figure 4a,b are the original interferogram and the simulation result of standard MLP, respectively. For the areas where the gross errors existed, the model provided a smooth result without changing its original characteristics, which indirectly indicates that the standard MLP had a weak ability to resist gross errors. Figure 4c,d are the result after gross error mask and the simulation result of EiMLP, respectively. The main phase jump regions were successfully identified and masked accordingly. Finally, a relatively reliable result was obtained through the special MLP layer in this study.

3.3. Comparison of the Corrected Phase

Taking the interferogram pair 20190911–20191005 as an example, the comparison of the corrected phases by four different methods was shown in Figure 5. Figure 5f–j present the phase histograms before and after correction using different methods. It can be clearly seen that the phase corrected by EiMLP was more concentrated around zero than those from other methods, with the lowest standard deviation (STD) of 0.628 rad. Furthermore, Figure 5k–o display the phase–elevation scatter diagrams. Although the global linear model achieved a correlation coefficient close to that of EiMLP, it exhibited a much larger phase standard deviation and higher phase dispersion. By contrast, the EiMLP method achieved the narrowest range of phase variation.

Another interferogram pair 20210620–20210702 was also selected to validate the proposed method. The original differential phase (Figure 6a) was severely contaminated by vertically stratified tropospheric delays and noise, which limited the correction performance of the global linear model, GACOS and standard MLP, as shown in Figure 6b–d. Figure 6f–j present the phase histograms before and after correction, along with the corresponding standard deviation (STD). Compared with the original phase, global linear model, GACOS,

and standard MLP, the STD reductions in EiMLP reached 86.48%, 77.50%, 52.16%, and 8.28%, respectively. Similar to Figure 5k–o, Figure 6k–o show the phase–elevation scatter diagrams for these phases, where the green line represents the linear regression fitting result.

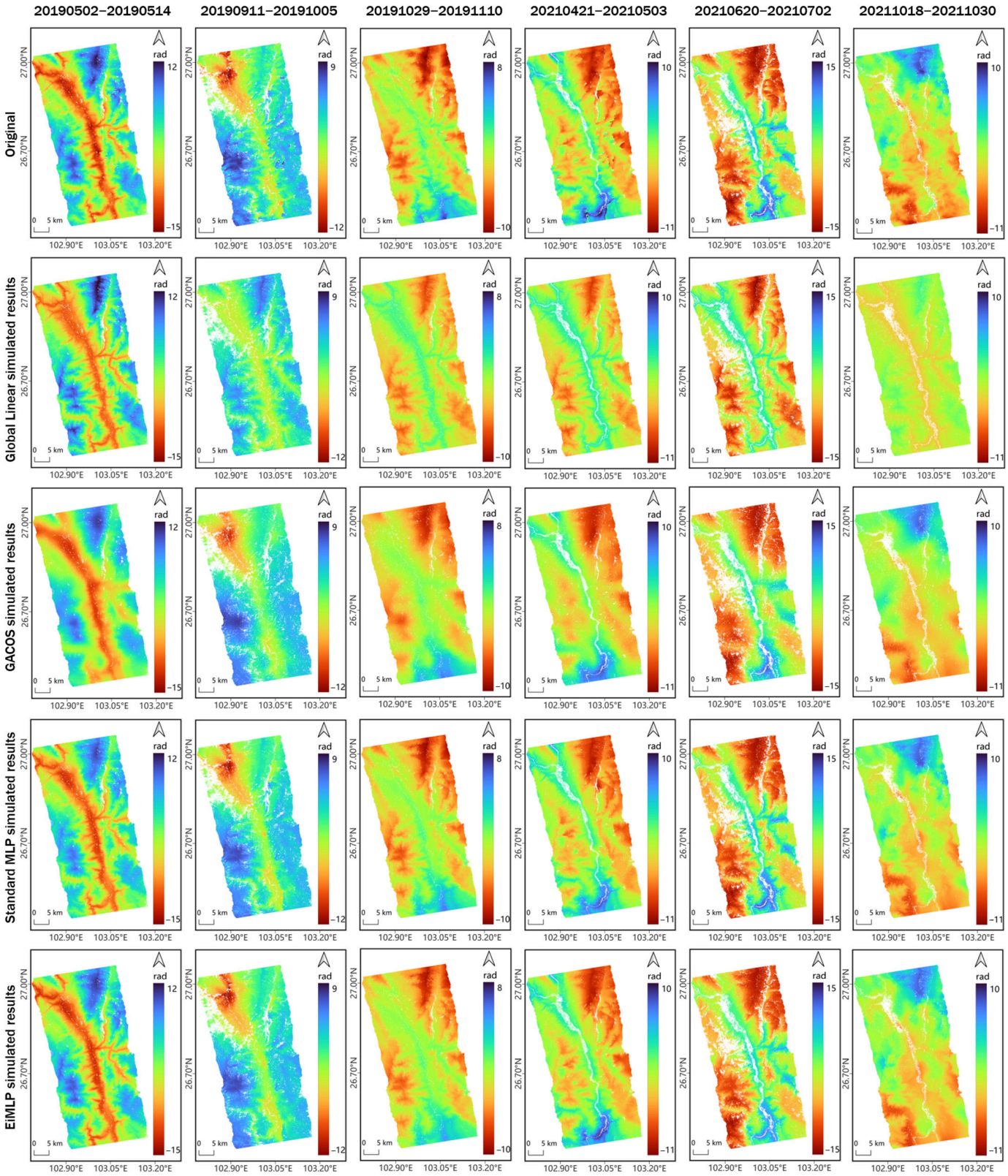


Figure 3. Comparison of the simulated phase by four different methods. Rows 1 to 5 correspond to the original atmospheric phase and the simulated phases obtained from the global linear model, GACOS, standard MLP, and EiMLP, respectively.

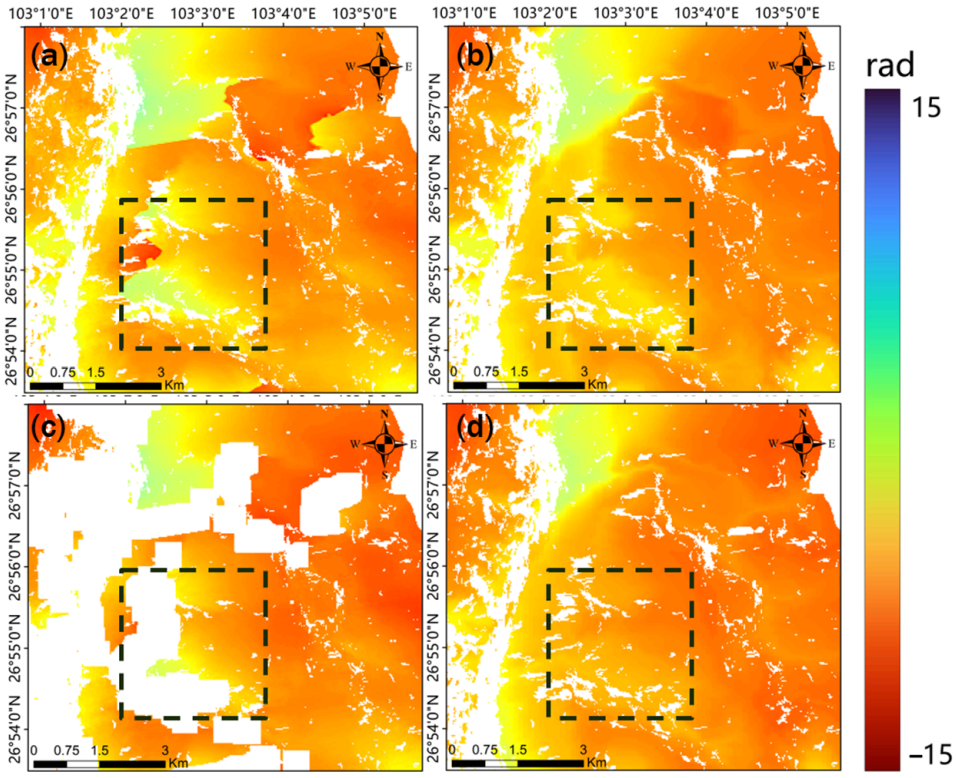


Figure 4. Comparison of local differences between the simulation results of interferograms interferogram pair 20210620–20210702. (**a**) Original interferogram, (**b**) simulation result of standard MLP, (**c**) result after gross error mask, (**d**) simulation result of EiMLP.

Table 3 summarizes the standard deviation (STD) and correlation coefficient of all interferograms, with the corresponding mean values listed in the last row. The STD values of the original phase and the corrected phases by the global linear model, GACOS, standard MLP, and EiMLP were 3.689 rad, 2.457 rad, 1.107 rad, 0.658 rad, and 0.629 rad, respectively. The corresponding correlation coefficients were 0.675, 0.009, 0.245, 0.139, and 0.079, respectively. Overall, the EiMLP method achieved the most stable STD and maintained the lowest phaseelevation correlation. Combining the results from Figures 7 and 8, it could be seen that the STD of the phase corrected by EiMLP showed a steady downward trend and was lower than that of the global linear model and GACOS. Although the proposed gross error identification module did not always reduce the STD, the STD of the EiMLP method remained at a relatively low level. Furthermore, the main advantage of this gross error identification module was also reflected in the subsequent deformation calculation.

3.4. Displacement Identification After Correction

The ultimate goal of atmospheric phase correction is to obtain high-precision surface deformation. Atmospheric delays in the study area tend to mask subtle deformation signals and may even be misinterpreted as surface displacement in regions with no actual ground movement. In this study, two interferogram pairs (20190911–20191005 and 20210620–20210702), which were most severely affected by atmospheric artifacts in the Baihetan Hydropower Station area, were selected for atmospheric correction using the four aforementioned methods. Surface deformation was subsequently estimated from the corrected interferograms, and three typical regions were chosen for detailed analysis.

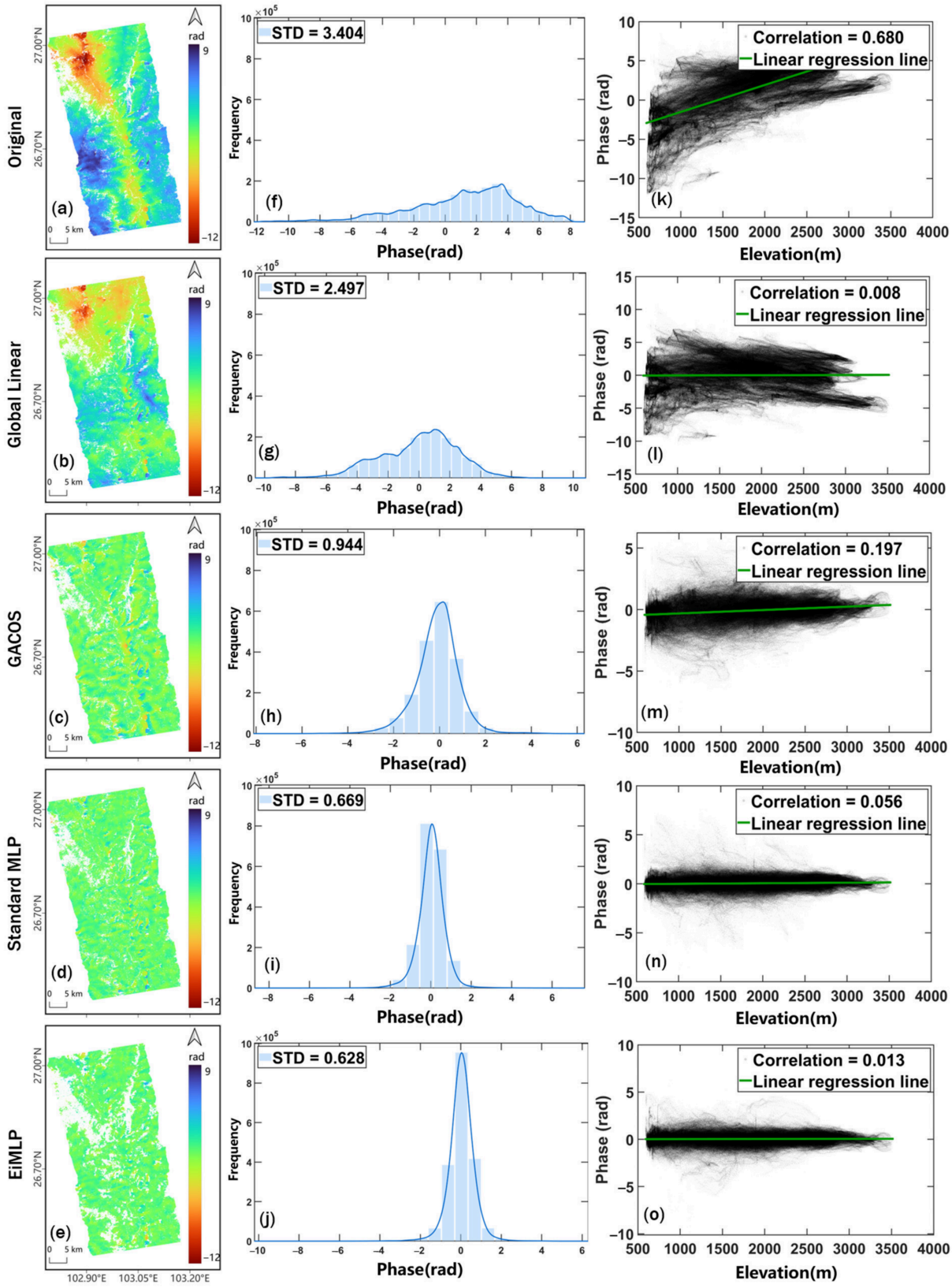


Figure 5. Comparison of the corrected phases of the interferogram pair 20190911–20191005 by four different methods. (**a**–**e**) Original, global linear-corrected, GACOS-corrected, standard MLP-corrected, and EiMLP-corrected phase, respectively. (**f**–**j**) The corresponding histograms of the phases (**a**–**e**) and standard deviation. (**k**–**o**) The phase–elevation scatter plots for the phases (**a**–**e**).

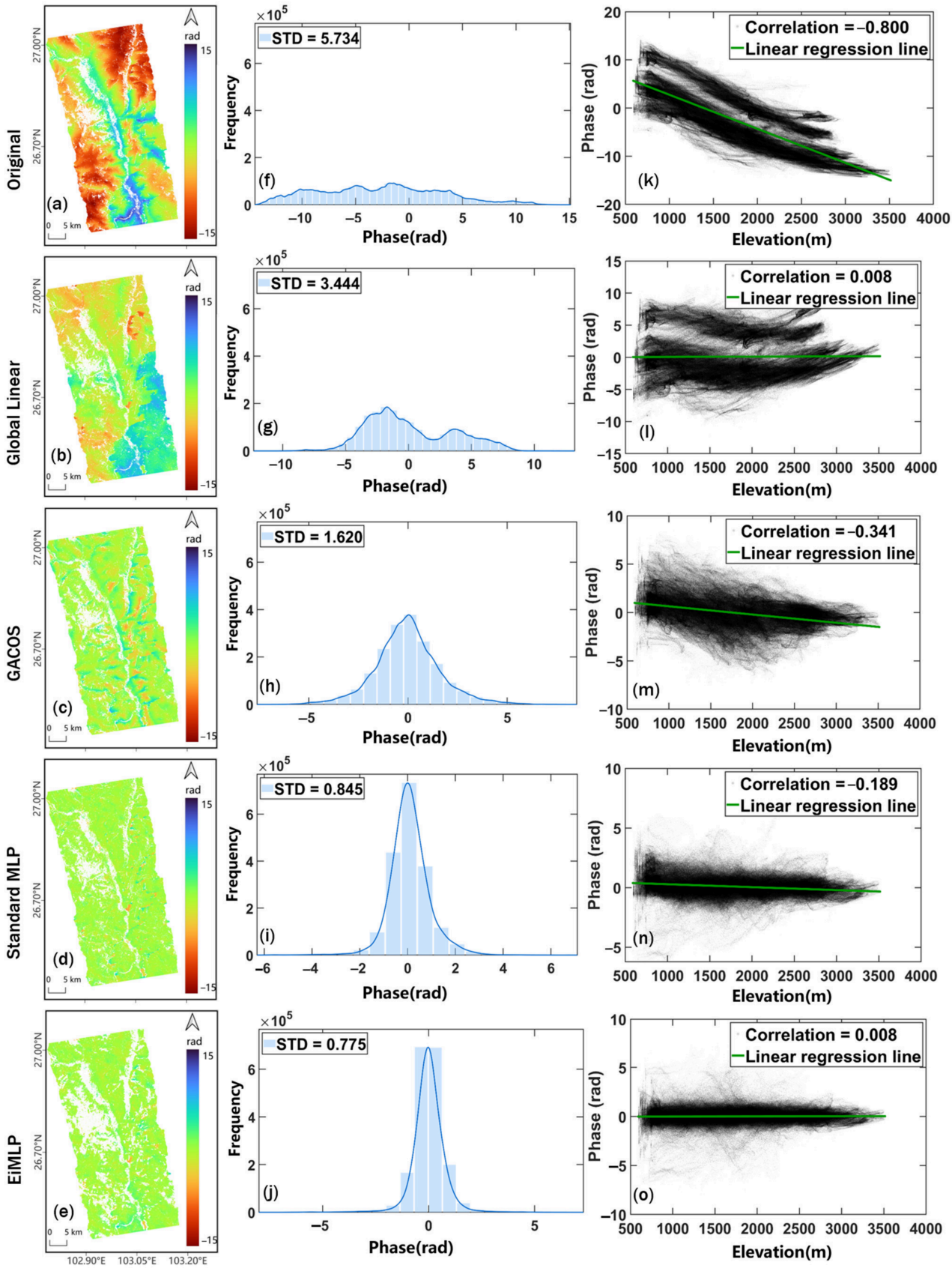


Figure 6. Comparison of the corrected phases of the interferogram pair 20210620–20210702 by four different methods. (**a**–**e**) Original, global linear-corrected, GACOS-corrected, standard MLP-corrected, and EiMLP-corrected phase, respectively. (**f**–**j**) The corresponding histograms of the phases (**a**–**e**) and standard deviation. (**k**–**o**) The phase–elevation scatter plots for the phases (**a**–**e**).

Table 3. Phase Std and correlation statistics after interferogram corrections.

Interferogram Pairs	Original		Global Linear		GACOS		Standard MLP		EiMLP	
	STD	Correlation	STD	Correlation	STD	Correlation	STD	Correlation	STD	Correlation
20190502–20190514	5.460	0.952	1.679	0.002	1.630	0.316	0.735	0.322	0.708	0.107
20190502–20190526	2.981	0.88	1.418	0.011	1.155	0.278	0.581	0.069	0.582	0.147
20190526–20190607	3.719	0.935	1.316	0.002	1.307	0.331	0.613	0.137	0.691	0.142
20190526–20190619	2.380	0.404	2.177	0.0001	1.054	0.171	0.597	0.072	0.627	0.025
20190619–20190701	3.214	0.815	1.864	−0.014	1.164	0.238	0.711	−0.08	0.684	−0.0005
20190806–20190818	4.871	0.663	3.648	0.011	1.127	0.265	0.629	0.207	0.591	0.068
20190806–20190830	4.745	0.807	2.800	0.008	1.506	0.237	0.856	0.092	0.820	0.035
20190911–20190923	7.685	0.703	5.463	0.003	1.601	0.253	0.929	0.127	0.953	0.138
20190911–20191005	3.404	0.68	2.497	0.008	0.944	0.197	0.628	0.056	0.669	0.013
20190923–20191005	4.463	0.894	2.002	0.009	1.271	0.349	0.562	0.128	0.640	0.18
20191005–20191017	2.424	0.582	1.971	0.008	0.856	0.162	0.586	0.043	0.609	0.05
20191017–20191029	4.153	0.719	2.886	0.008	1.145	0.273	0.626	0.031	0.696	0.079
20191017–20191110	2.066	0.593	1.740	0.013	0.726	0.209	0.449	0.094	0.395	0.061
20191029–20191110	2.568	0.719	1.784	0.004	0.731	0.248	0.529	0.272	0.471	0.061
20191029–20191122	2.419	0.884	1.129	0.005	0.961	0.267	0.624	0.168	0.536	0.122
20210421–20210503	3.413	0.703	2.427	0.011	1.055	0.28	0.709	0.046	0.611	0.029
20210503–20210515	3.022	0.546	2.532	0.002	0.866	0.107	0.420	0.204	0.463	0.038
20210503–20210527	6.105	0.926	2.310	0.006	1.619	0.34	0.962	0.38	0.895	0.167
20210527–20210608	4.281	0.816	2.476	0.008	1.496	0.316	0.771	0.317	0.720	0.142
20210608–20210620	3.733	0.869	1.846	0.01	1.164	0.314	0.683	0.235	0.572	0.165
20210608–20210702	2.121	0.616	1.743	0.019	0.773	0.259	0.397	0.082	0.444	0.067
20210620–20210702	5.734	0.8	3.444	0.008	1.620	0.341	0.845	0.189	0.775	0.008
20210807–20210819	3.248	0.649	2.472	0.042	0.941	0.272	0.533	0.086	0.517	0.093
20210807–20210831	2.567	0.243	2.492	0.032	0.719	0.07	0.499	0.017	0.527	0.02
20210809–20210831	2.010	0.706	1.423	0.001	0.856	0.249	0.473	0.076	0.492	0.006
20210912–20210924	5.193	0.299	4.956	0.0001	1.350	0.23	0.749	0.159	0.836	0.034
20210912–20211006	4.010	0.231	3.902	0.015	1.196	0.148	0.728	0.047	0.815	0.103
20211018–20211030	3.041	0.395	2.795	0.007	0.747	0.14	0.423	0.094	0.472	0.043
Mean	3.751	0.679	2.471	0.008	1.128	0.245	0.637	0.131	0.636	0.076

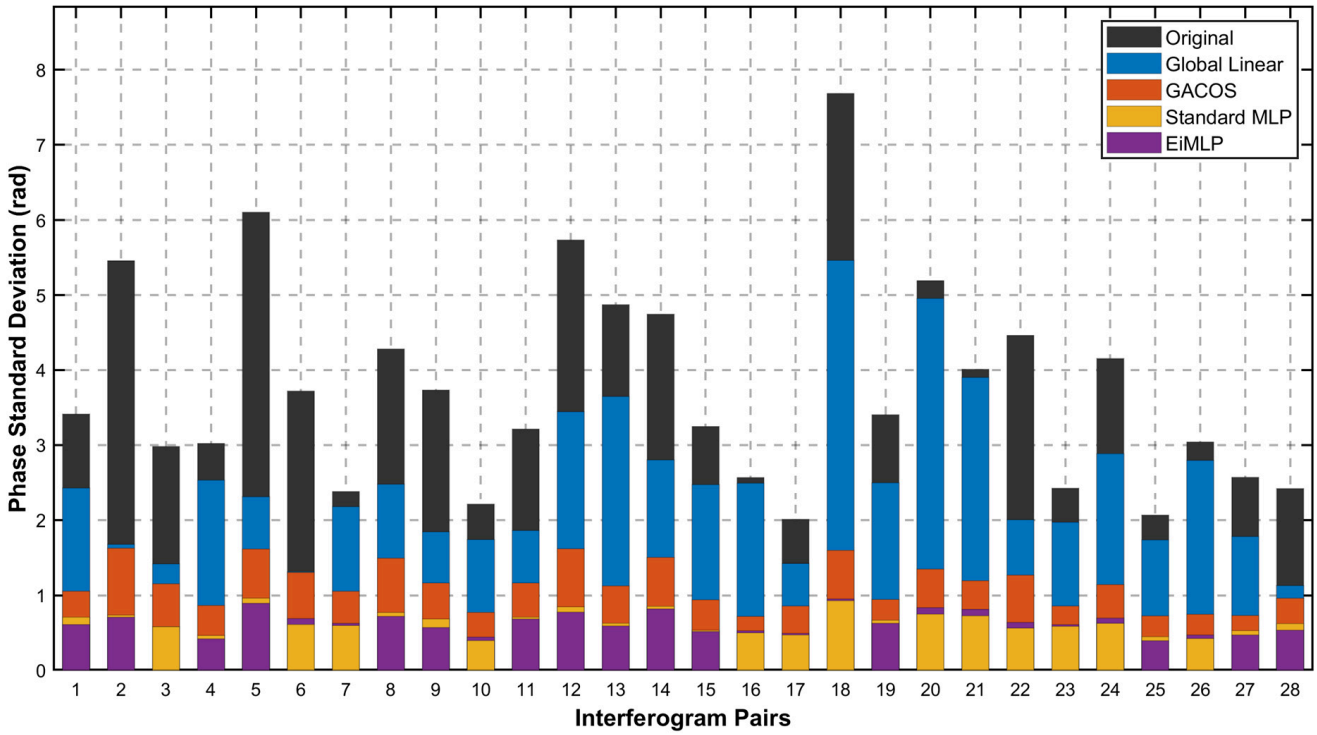


Figure 7. Comparison of STD results before and after the correction for each model.

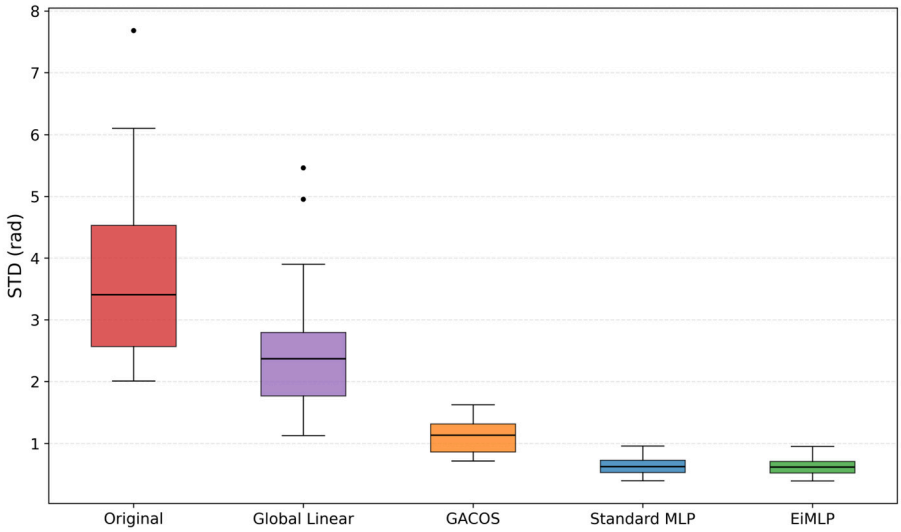


Figure 8. Comparison of the STDs of all interferograms before and after correction by different methods. The black dots represent the outliers, which beyond the range of the upper and lower bounds.

Region A corresponds to a specific area in interferogram pair 20210620–20210702. Based on optical remote sensing images (Figure 9f), no obvious deformation pattern was observed at this region, yet the original deformation results were anomalous due to severe atmospheric errors. As shown in Figure 9a, an apparent positive LOS displacement (approximately 21.1 mm) was observed in the deformation derived from the original phase, which could be misinterpreted as a movement toward the satellite along the LOS direction. Although the deformations estimated from corrected phases by the global linear model and GACOS were partially reduced, the spurious positive signal still remained. After the correction by the standard MLP and EiMLP methods, the spurious component was substantially eliminated, and the influence of atmospheric delay errors became negligible. In particular, the deformation derived from the EiMLP-corrected phase was only 1.38 mm (Figure 9e).

Regions B and C were identified as typical deformation zones from interferogram pair 20190911–20191005, and these areas were also documented in references [35,36]. Region B, situated on the riverbank of the Jinsha River, was analyzed in Figure 10. The deformation derived from the original phase (Figure 10a) was severely distorted by phase unwrapping errors. Similarly, the deformation results obtained from the global linear model, GACOS, and standard MLP (Figure 10b–d) were also compromised by phase unwrapping errors. In contrast, the EiMLP-corrected result delineated a clearer and more spatially continuous deformation boundary (Figure 10e), which effectively suppressed phase unwrapping errors to nearly undetectable levels. As shown in Figure 10e,f, the area with notable LOS displacement outlined by the blue dashed line was located in the central section of the detected deformation feature, with a displacement of approximately −7.4 mm.

Region C was a suspected landslide zone located in a valley surrounded by mountains on three sides, with an opening to the west. The deformation derived from the original phase was clearly affected by both unwrapping errors and atmospheric delays, with a deformation of −14.2 mm. The deformation after global linear and GACOS correction was similar to the results of the original phase, accompanied by boundary discontinuities. The deformation derived from standard MLP correction was also unreliable and severely affected by unwrapping errors. As illustrated in Figure 11e,f, the deformation derived from EiMLP correction revealed a more spatially continuous pattern. The area with notable LOS displacement outlined by the blue dashed line exhibited smooth boundary transitions and negligible atmospheric artifacts, with a displacement of approximately −15.2 mm.

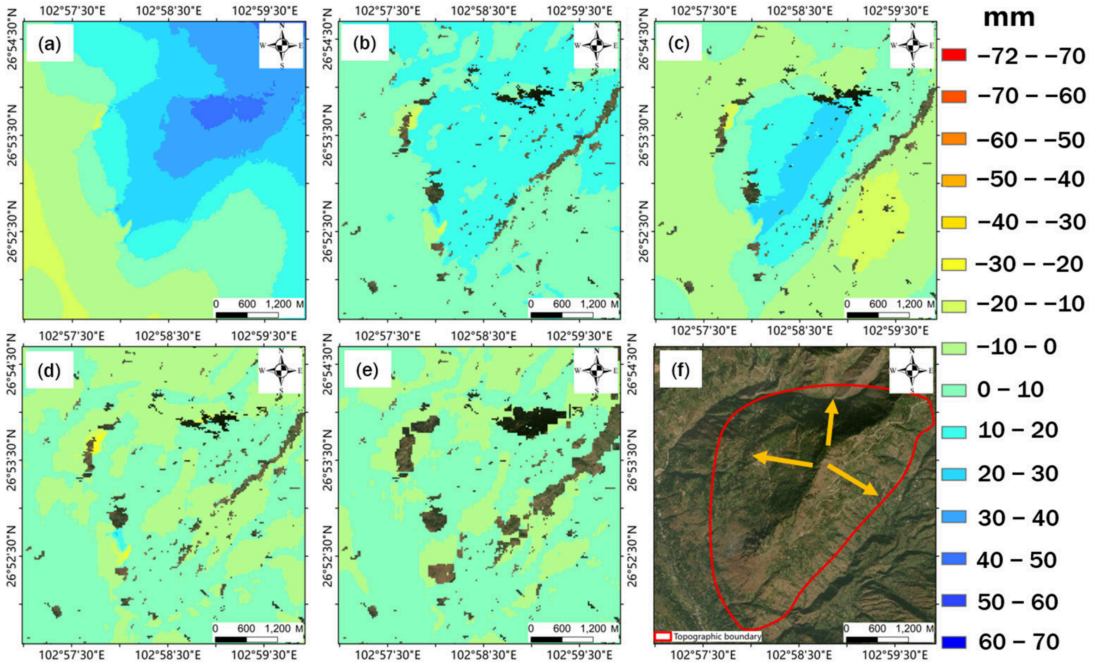


Figure 9. Detailed deformation results of Region A. (**a**) Original deformation with atmospheric effects; (**b**) linear model-corrected deformation; (**c**) GACOS-corrected deformation; (**d**) MLP-corrected deformation; (**e**) EiMLP-corrected deformation; (**f**) remote sensing imagery of Region A. It is noted that the arrow indicates the downhill direction.

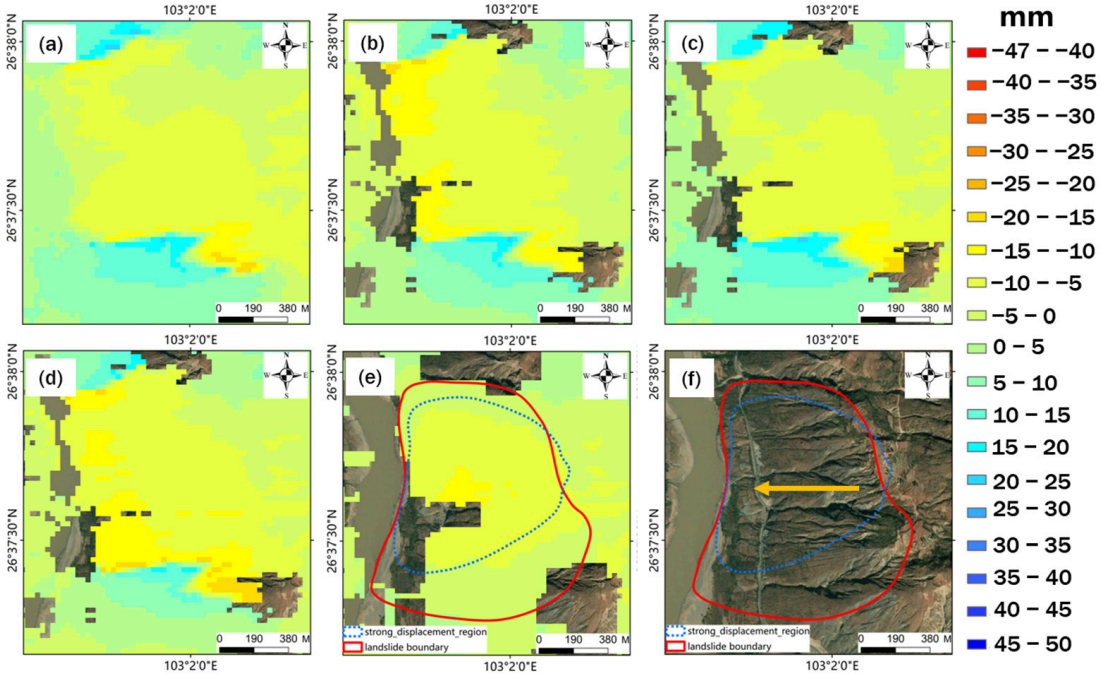


Figure 10. Detailed deformation results of Region B. (**a**) Original deformation with gross error, (**b**) linear model-corrected deformation, (**c**) GACOS-corrected deformation, (**d**) MLP-corrected deformation, (**e**) EiMLP-corrected deformation, (**f**) remote sensing imagery of the deformed area. It is noted that the arrow indicates the downhill direction.

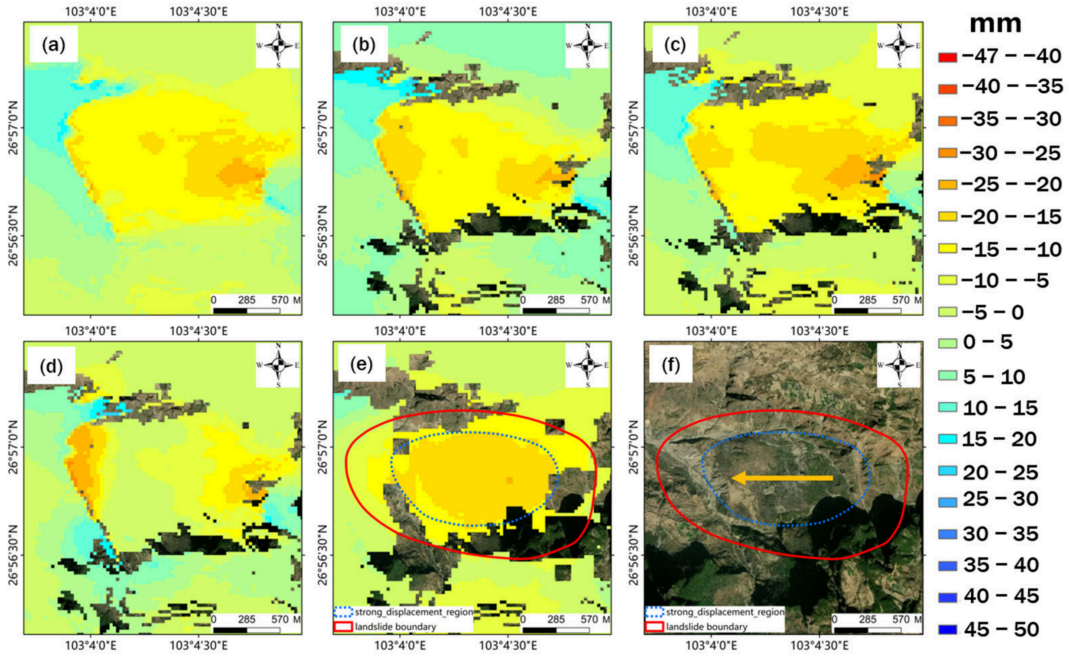


Figure 11. Detailed deformation results of Region C. (**a**) Original deformation with gross error, (**b**) linear model-corrected deformation, (**c**) GACOS-corrected deformation, (**d**) MLP-corrected deformation, (**e**) EiMLP-corrected deformation, (**f**) remote sensing imagery of the deformed area. It is noted that the arrow indicates the downhill direction.

4. Discussion

4.1. Model Parameter Settings

The GPU equipped in this study was the NVIDIA GeForce RTX 2060 with 6 GB of video memory. Figure 12 shows the time consumption of the EiMLP model for tropospheric delay correction under different parameters. When the sliding window size was set to 10 and 20, both the model training time and the reconstruction time of the tropospheric delay phase were reduced by approximately 30 s. Among these, a window size of 5 combined with a threshold of 2.0 took the longest time, reaching 480 s for a single interferogram.

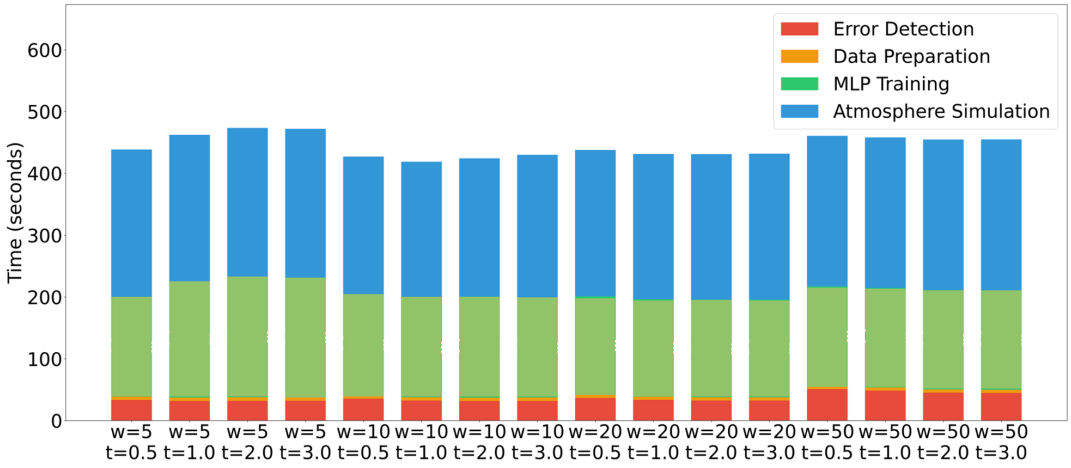


Figure 12. Time consumption statistics of the error correction process under different parameter settings.

Taking interferogram pair 20210620–20210702 as an example, the comparison of SSIM under different combinations of window size and threshold parameters is shown in Figure 13. When the window size was 10 and the threshold was 1, the statistical indicators

of the simulation results were the best and the phase standard deviation of the corrected interferogram was the lowest (Figure 14). Since the situations of different interferograms varied, a threshold of 1 might lead to missed detections or partial false detections. Moreover, in some cases, the correction results were better when the window size was set to 5 or 20 and the threshold was set to 1.0 or 2.0. In future work, a more comprehensive evaluation system would be established based on statistical indicators to determine relatively stable parameter configurations for experiments involving a large number of interferograms.

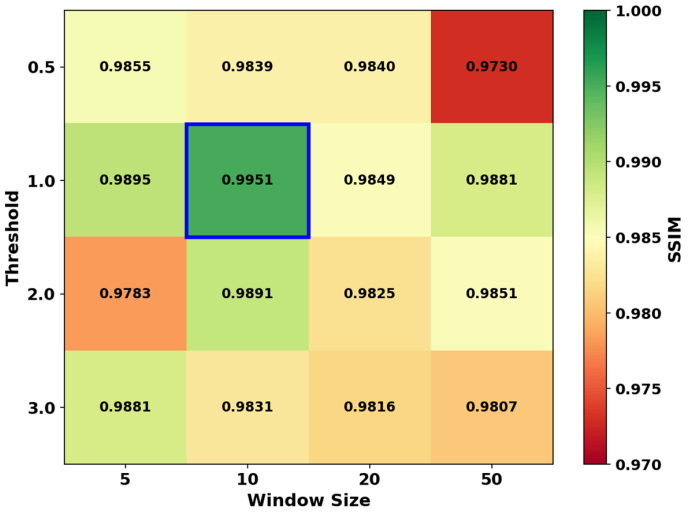


Figure 13. Comparison of SSIM results based on different parameters. It is noted that the blue square denotes the maximum SSIM value.

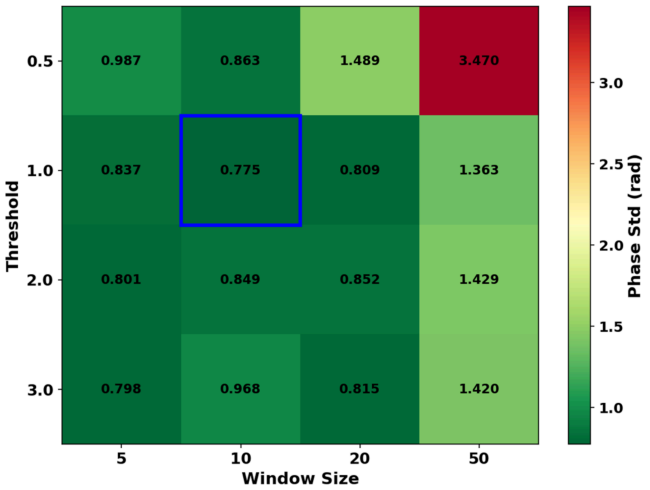


Figure 14. Comparison of phase standard deviation after correction with different parameters. It is noted that the blue square denotes the minimum phase std value.

4.2. The Instability of EiMLP Correction

(1) The limitations of masking

As mentioned in Section 3.3, the phase STD results after EiMLP correction were not always optimal. Several interferogram pairs whose phase standard deviation after standard MLP correction was lower than that of the EiMLP results were selected for detail analysis (Figure 15). It can be seen that the masked areas mainly covered the steep mountainous regions on both sides of the Jinsha River, which was also the main area where tropospheric delay occurred. Large-scale masks led to the loss of a large number of samples containing tropospheric delay, thereby reducing the accuracy of the model in simulating tropospheric delay.

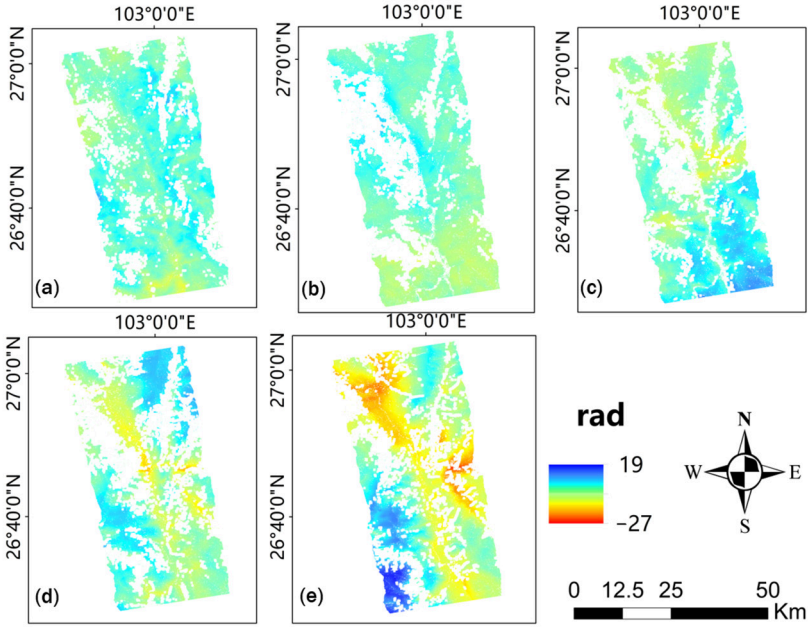


Figure 15. Interferograms after gross error mask. (**a**–**e**) Interferogram pairs 20190526–20190619, 20210807–20210831, 20210912–20211006, 20190923–20191005, 20190911–20190923, respectively.

(2) Limitations of deformation calculation just based on ascending Sentinel-1A data

In this study, the azimuth angle and the incidence angle of the ascending Sentinel-1A data is approximately 347.5° and 39.8°, respectively. Under this viewing geometry, it is highly sensitive to east–west movements, but not sensitive to north–south movements. Figure 16a shows the overall slope aspect of the study area, indicating that the overall slope aspect is mainly east–west, with only a small amount of north–south slope. Except for region A, which was surrounded by mountains with only a small scale of north-facing slope, the slope aspect of the other areas was mainly westward. It might lead to the neglect of some north–south deformations. However, the sensitivity of the LOS to upward movement was approximately 0.87; it could be concluded that it was sufficiently sensitive for the analysis of deformation just based on the ascending SAR data in this study area.

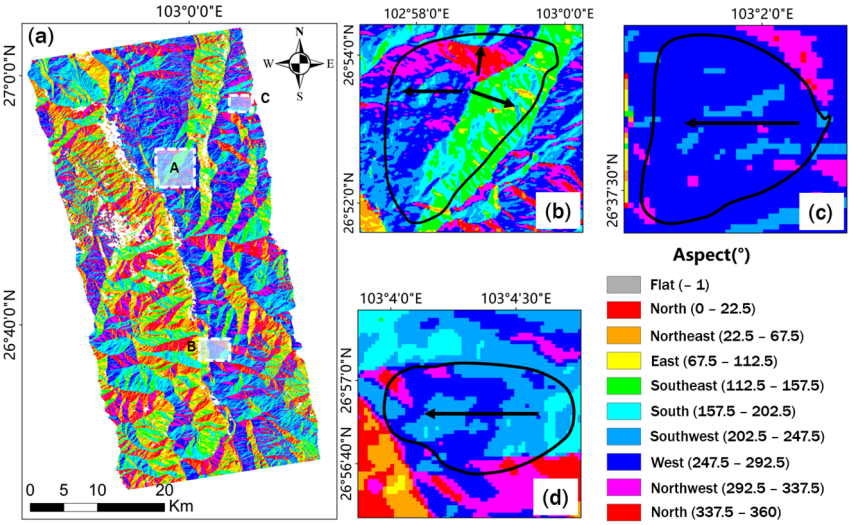


Figure 16. (**a**) The overall slope aspect of the study area; (**b**–**d**) the enlarged maps of the slopes in the selected areas (A–C) described in this study. The black polygon represents the boundary of the topography(deformation), and the arrow indicates the downhill direction.

5. Conclusions

To mitigate the impact of tropospheric delays in interferograms while reducing the high dependence of deep learning models on phase unwrapping results, this study proposed a tropospheric delay correction method (EiMLP) that integrated gross error identification with the MLP algorithm. The EiMLP model was applied to 30 ascending Sentinel-1A SAR images acquired over the Baihetan Hydropower Station area, and its performance was compared with the global linear model, GACOS, and standard MLP method in terms of tropospheric delay simulation and correction. The main conclusions are summarized as follows:

(1) The proposed EiMLP model effectively eliminates most of the tropospheric delay errors, and has a good correction performance on all interferograms. The standard deviation (STD) of the interferogram phase after correction decreased by an average of 83%, and the average phase–elevation correlation coefficient after correction was 0.076, indicating that the corrected phase was basically independent of elevation. After the EiMLP correction, the lower phase–elevation correlation indicated that the influence of tropospheric delay affected by terrain was weakened, thus enabling weak deformation signals to be effectively separated from the residuals. In addition, the proposed method requires no external auxiliary data for tropospheric delay correction and can accurately correct individual interferograms in mountainous regions with complex terrain.

(2) The gross error identification module is adopted to mitigate the reliance of the MLP training process on the quality of phase unwrapping. Comparative experiments between the standard MLP and EiMLP demonstrate that uncorrected unwrapping gross errors compromise the reliability of deformation calculation, typically characterized by abrupt phase boundaries between adjacent pixels. The proposed gross error identification method exhibits high sensitivity to such anomalies, enabling the effective detection and elimination of these error-prone regions.

However, it is worth noting that the EiMLP model has several limitations. The method relies to a certain extent on prior knowledge, particularly the setting of the phase gradient threshold. When applied to longer-baseline interferograms under more complex conditions, the proposed gross error identification module may generate excessive masking, resulting in suboptimal correction performance. Furthermore, the future application of the model to time-series processing needs to account for more complex factors such as turbulent delay and data gaps, and the weights of the loss function may require appropriate adjustment. To overcome these shortcomings, future research will focus on further optimizing the model architecture and will also integrate more diverse experimental data.

Author Contributions: Conceptualization, Y.L. and H.C.; methodology, Y.L. and H.C.; software, H.C.; validation, Y.L. and H.C.; formal analysis, Y.L.; investigation, D.L. and B.L.; resources, Y.L. and D.L.; data curation, Y.L.; writing—original draft preparation, H.C.; writing—review and editing, Y.L., D.L. and B.L.; visualization, H.C.; supervision, Y.L.; project administration, H.C.; funding acquisition, Y.L., D.L. and B.L. All authors have read and agreed to the published version of the manuscript.

Funding: This research was funded by the National Natural Science Foundation of China (No. 42104030, 42161064), and the Jiangxi Provincial Natural Science Foundation (No. 20232BAB213054).

Institutional Review Board Statement: Not applicable.

Informed Consent Statement: Not applicable.

Data Availability Statement: The Sentinel-1 data used for this study are available in publicly accessible web links: https://search.asf.alaska.edu/ (accessed on 26 February 2026), https://dataspace.copernicus.eu/ (accessed on 26 February 2026), and https://www.gacos.net/ (accessed on 7 March 2026).

Acknowledgments: The authors would like to thank the European Space Agency (ESA) for providing the Sentinel-1 SAR images and the Copernicus Digital Elevation Model. The authors would also like to thank the Generic Atmospheric Correction Online Service for InSAR (GACOS) (https://www.gacos.net/, accessed on 7 March 2026) for providing datasets.

Conflicts of Interest: The authors declare no conflicts of interest.

References

1. Rosi, A.; Tofani, V.; Tanteri, L.; Tacconi Stefanelli, C.; Agostini, A.; Catani, F.; Casagli, N. The new landslide inventory of Tuscany (Italy) updated with PS-InSAR: Geomorphological features and landslide distribution. *Landslides* **2018**, *15*, 5–19. [CrossRef]
2. Liu, Y.; Yao, X.; Gu, Z.; Li, R.; Zhou, Z.; Liu, X.; Jiang, S.; Yao, C.; Wei, S. Research on automatic recognition of active landslides using InSAR deformation under digital morphology: A case study of the Baihetan reservoir. *China Remote Sens. Environ.* **2024**, *304*, 114029. [CrossRef]
3. Zang, Z.; Zhao, C.; Yan, M.; Liu, X.; Yang, C.; Peng, P.; Wei, Y. Detection of landslides in the southwestern Qingzang Plateau using both LuTan-1 and Sentinel-1 SAR Images. *Sci. Surv. Mapp.* **2025**, *50*, 42–54.
4. Ryder, I.; Parsons, B.; Wright, T.; Funning, G. Post-seismic motion following the 1997 Manyi (Tibet) earthquake: InSAR observations and modelling. *Geophys. J. Int.* **2007**, *169*, 1009–1027. [CrossRef]
5. Mangum, J.; Wallace, P. Atmospheric refractive electromagnetic wave bending and propagation delay. *Publ. Astron. Soc. Pac.* **2015**, *127*, 74–91. [CrossRef] [PubMed]
6. Zhang, S.; Song, M.; Luo, Y.; Lei, K.; Liu, W.; Pang, X. Research on tropospheric delay correction for time series InSAR. *Sci. Surv. Mapp.* **2021**, *46*, 108–117.
7. Wu, Y.; Li, Z.H.; Liu, J.; Xu, C. Atmospheric correction models for InSAR measurements. *Geomat. Inf. Sci. Wuhan Univ.* **2006**, *31*, 862–867.
8. Yan, Z.; Li, Z. Comparison of atmospheric water vapor correction models for InSAR measurements. *Geomat. Inf. Sci. Wuhan Univ.* **2008**, *33*, 723–726.
9. Zhang, C.; Li, Z.; Yu, C.; Song, C.; Xiao, R.; Peng, J. Landslide detection of the Jinsha river region using GACOS assisted InSAR stacking. *Geomat. Inf. Sci. Wuhan Univ.* **2021**, *46*, 1649–1657.
10. Bock, Y.; Williams, S. Integrated satellite interferometry in southern California. *Eos Trans. AGU.* **1997**, *78*, 293–300. [CrossRef]
11. Hanssen, R.F.; Lehner, S.; Weinreich, I. Atmospheric heterogeneities in ERS tandem SAR interferometry. In *Proceeding of the CEOS SAR Workshop*; ESTEC: Noordwijk, The Netherlands, 1998.
12. Wu, S.; Liu, G.; Jia, H.; Zhang, B.; Zhang, R.; Mao, W.; Wu, T. An InSAR atmospheric correction method based on GNSS and machine learning. *Geomat. Inf. Sci. Wuhan Univ.* **2025**, *50*, 1864–1877.
13. Yan, H.; Lu, Z.; Li, Y.; Wang, R.; Li, F.; Tang, Q. InSAR atmospheric error correction method based on GNSS spatial interpolation with application to the Southern North Island of New Zealand. *IEEE Trans. Geosci. Remote Sens.* **2025**, *64*, 4100815. [CrossRef]
14. Dong, J.; Zhang, L.; Liao, M.; Gong, J. Improved correction of seasonal tropospheric delay in InSAR observations for landslide deformation monitoring. *Remote Sens. Environ.* **2019**, *233*, 111370. [CrossRef]
15. Hetland, E.A.; Musé, P.; Simons, M.; Lin, Y.; Agram, P.S.; DiCaprio, C.J. Multiscale InSAR time series (MInTS) analysis of surface deformation. *J. Geophys. Res. Solid Earth* **2012**, *117*, B02404. [CrossRef]
16. Dai, W.; Liu, N.; Santerre, R.; Pan, J. Dam deformation monitoring data analysis using space-time Kalman filter. *ISPRS Int. J. Geo-Inf.* **2016**, *5*, 236. [CrossRef]
17. Sandwell, D.T.; Price, E.J. Phase gradient approach to stacking interferograms. *J. Geophys. Res. Solid Earth* **1998**, *103*, 30183–30204. [CrossRef]
18. He, X.; Li, Z.; Mu, M.; Duan, M.; Wei, J.; Cao, Y. Refining stacking-InSAR by considering the statistical characteristics of atmospheric turbulence. *IEEE Trans. Geosci. Remote Sens.* **2024**, *62*, 5215714. [CrossRef]
19. Chen, H.; Shen, Y.; Zhang, L.; Liang, H.; Feng, T.; Song, X. Mitigation of tropospheric turbulent delays in InSAR time series by incorporating a stochastic process. *ISPRS J. Photogramm. Remote Sens.* **2025**, *222*, 186–203. [CrossRef]
20. Liu, N.; Wu, H.; Zhang, Y.; Zhang, L.; Yang, A.; Kang, Y.; Wei, J.; Deng, L. Joint spatio-temporal correction for both turbulent and vertically stratified delays in time series SAR interferometry. *IEEE J. Sel. Top. Appl. Earth Obs. Remote Sens.* **2026**, *19*, 8898–8913. [CrossRef]
21. Shi, M.; Peng, J.; Chen, X.; Zheng, Y.; Yang, H.; Su, Y.; Wang, G.; Wang, W. An improved method for InSAR atmospheric phase correction in mountainous areas. *IEEE J. Sel. Top. Appl. Earth Obs. Remote Sens.* **2021**, *14*, 10509–10519. [CrossRef]
22. Zhao, Y.; Zuo, X.; Li, Y.; Guo, S.; Bu, J.; Yang, Q. Evaluation of InSAR tropospheric delay correction methods in a low-latitude alpine canyon region. *Remote Sens.* **2023**, *15*, 990. [CrossRef]
23. Refice, A.; Belmonte, A.; Bovenga, F.; Pasquariello, G. On the use of anisotropic covariance models in estimating atmospheric DInSAR contributions. *IEEE Geosci. Remote Sens. Lett.* **2010**, *8*, 341–345. [CrossRef]

24. Wei, J.; Li, Z.; Hu, J.; Feng, G.; Duan, M. Anisotropy of atmospheric delay in InSAR and its effect on InSAR atmospheric correction. *J. Geod.* **2019**, *93*, 241–265. [CrossRef]
25. Xie, L.; Ma, Z.; Xu, W.; Zhao, W. A quadtree wavelet multiresolution approach for InSAR heterogeneous topography-correlated tropospheric delay correction in mountainous landslide monitoring. *IEEE J. Sel. Top. Appl. Earth Obs. Remote Sens.* **2026**, *19*, 1404–1414. [CrossRef]
26. Mulder, G.; Leijen, F.J.V.; Hanssen, R.F. A generic approach to parameterize the turbulent energy of single-epoch atmospheric delays from InSAR time-series. *IEEE Trans. Geosci. Remote Sens.* **2023**, *61*, 5212413. [CrossRef]
27. Chen, Y.; Bruzzone, L.; Jiang, L.; Sun, Q. ARU-net: Reduction of atmospheric phase screen in SAR interferometry using attention-based deep residual U-net. *IEEE Trans. Geosci. Remote Sens.* **2020**, *59*, 5780–5793. [CrossRef]
28. Zhao, Z.; Wu, Z.; Zheng, Y.; Ma, P. Recurrent neural networks for atmospheric noise removal from InSAR time series with missing values. *ISPRS J. Photogramm. Remote Sens.* **2021**, *180*, 227–237. [CrossRef]
29. Ma, P.; Yu, C.; Jiao, Z.; Zheng, Y.; Wu, Z.; Mao, W.; Lin, H. Improving time-series InSAR deformation estimation for city clusters by deep learning-based atmospheric delay correction. *Remote Sens. Environ.* **2024**, *304*, 114004. [CrossRef]
30. Chen, C.; Dai, K.; Tang, X.; Cheng, J.; Pirasteh, S.; Wu, M.; Shi, X.; Zhou, H.; Li, Z. Removing InSAR topography-dependent atmospheric effect based on deep learning. *Remote Sens.* **2022**, *14*, 4171. [CrossRef]
31. Zhou, H.; Dai, K.; Tang, X.; Xiang, J.; Li, R.; Wu, M.; Peng, Y.; Li, Z. Time-series InSAR with deep-learning-based topography-dependent atmospheric delay correction for potential landslide detection. *Remote Sens.* **2023**, *15*, 5287. [CrossRef]
32. Zhou, H.; Dai, K.; Pirasteh, S.; Li, R.; Xiang, J.; Li, Z. InSAR Spatial-Heterogeneity Tropospheric Delay Correction in Steep Mountainous Areas Based on Deep Learning for Landslides Monitoring. *IEEE Trans. Geosci. Remote Sens.* **2023**, *61*, 5215014. [CrossRef] [PubMed]
33. Zhu, S.; Yin, Y.; Wang, M.; Zhu, M.; Wang, C.; Wang, W.; Li, J.; Zhao, H. Instability mechanism and disaster mitigation measures of long-distance landslide at high location in Jinsha River junction zone: Case study of Sela landslide in Jinsha River, Tibet. *Chin. J. Geotech. Eng.* **2021**, *43*, 688–697. [CrossRef]
34. Zhang, R.; Zhao, X.; Dong, X.; Dai, K.; Deng, J.; Zhuo, G.; Yu, B.; Wu, T.; Xiang, J. Potential landslide identification in Baihetan Reservoir area based on C-/L-band synthetic aperture radar data and applicability analysis. *Remote Sens.* **2024**, *16*, 1591. [CrossRef]
35. Xiao, R.; Jiang, M.; Li, Z.; He, X. New insights into the 2020 Sardoba dam failure in Uzbekistan from Earth observation. *Int. J. Appl. Earth Obs. Geoinf.* **2022**, *107*, 102705. [CrossRef]
36. Wang, H.; Deng, C.; Zhang, Z.; Jiang, Z.; Wei, Q.; Yi, W.; Chen, T.; Ma, J. Dynamic Landslide Susceptibility Assessment Integrating SBAS-InSAR and Interpretable Machine Learning: A Case Study of the Baihetan Reservoir Area, Southwest China. *Remote Sens.* **2026**, *18*, 578. [CrossRef]
37. Li, Y.; Li, L.; Chen, C.; Liu, Y. Correction of global digital elevation models in forested areas using an artificial neural network-based method with the consideration of spatial autocorrelation. *Int. J. Digit. Earth* **2023**, *16*, 1568–1588. [CrossRef]
38. Tolstikhin, I.; Houlsby, N.; Kolesnikov, A.; Beyer, L.; Zhai, X.; Unterthiner, T.; Yung, J.; Steiner, A.; Keysers, D.; Uszkoreit, J.; et al. MLP-mixer: An all-MLP architecture for vision. *Adv. Neural Inf. Process. Syst.* **2021**, *34*, 24261–24272.
39. Doin, M.P.; Lasserre, C.; Peltzer, G.; Cavalié, O.; Doubre, C. Corrections of stratified tropospheric delays in SAR interferometry: Validation with global atmospheric models. *J. Appl. Geophys.* **2009**, *69*, 35–50. [CrossRef]
40. Delacourt, C. Tropospheric correction of SAR interferograms with strong topography: Application to Etna. *Geophys. Res. Lett.* **1998**, *25*, 2849–2852. [CrossRef]
41. Yu, C.; Li, Z.; Penna, N.T.; Crippa, P. Generic atmospheric correction model for interferometric synthetic aperture radar observations. *J. Geophys. Res. Solid Earth* **2018**, *123*, 9202–9222. [CrossRef]
42. Yu, C.; Li, Z.; Bai, L.; Muller, J.P.; Zhang, J.; Zeng, Q. Successful applications of generic atmospheric correction online service for InSAR (GACOS) to the reduction of atmospheric effects on InSAR observations. *J. Geod. Geoinf. Sci.* **2021**, *4*, 109–115. [CrossRef]
43. Zhang, X.; Li, Z.; Liu, Z. Reduction of atmospheric effects on InSAR observations through incorporation of GACOS and PCA into small baseline subset InSAR. *IEEE Trans. Geosci. Remote Sens.* **2023**, *61*, 5209115. [CrossRef]
44. Wang, Z.; Bovik, A.; Sheikh, H.R.; Simoncelli, E.P. Image quality assessment: From error visibility to structural similarity. *IEEE Trans. Image Process.* **2005**, *13*, 600–612. [CrossRef] [PubMed]

Disclaimer/Publisher's Note: The statements, opinions and data contained in all publications are solely those of the individual author(s) and contributor(s) and not of MDPI and/or the editor(s). MDPI and/or the editor(s) disclaim responsibility for any injury to people or property resulting from any ideas, methods, instructions or products referred to in the content.